REPORT DOCUMENTATION PAGE

Form Approved OMB No. 0704-0188

1. REPORT DATE *(DD-MM-YYYY)*: 20-12-2011

2. REPORT TYPE: Journal Article

3. DATES COVERED *(From - To)*:

4. TITLE AND SUBTITLE
Relationships Between Water Attenuation Coefficients Derived from Active and Passive Remote Sensing: A Case Study from Two Coastal Environments

5a. CONTRACT NUMBER:

5b. GRANT NUMBER:

5c. PROGRAM ELEMENT NUMBER: 0601153N

5d. PROJECT NUMBER:

5e. TASK NUMBER:

5f. WORK UNIT NUMBER: 73-9857-01-5

6. AUTHOR(S)
Martin Montes, J. Churnside, Zhongping Lee, Richard Gould, Robert Arnone, Alan Weidemann

7. PERFORMING ORGANIZATION NAME(S) AND ADDRESS(ES)
Naval Research Laboratory
Oceanography Division
Stennis Space Center, MS 39529-5004

8. PERFORMING ORGANIZATION REPORT NUMBER: NRL/JA/7330-11-0714

9. SPONSORING/MONITORING AGENCY NAME(S) AND ADDRESS(ES)
Office of Naval Research
800 N. Quincy St.
Arlington, VA 22217-5660

10. SPONSOR/MONITOR'S ACRONYM(S): ONR

11. SPONSOR/MONITOR'S REPORT NUMBER(S):

12. DISTRIBUTION/AVAILABILITY STATEMENT
Approved for public release, distribution is unlimited.

13. SUPPLEMENTARY NOTES

20120113182

14. ABSTRACT

Relationships between the satellite-derived diffuse attenuation coefficient of downwelling irradiance (Kd) and airborne-based vertical attenuation of lidar volume backscattering (α) were examined in two coastal environments. At 1.1 km resolution and a wavelength of 532 nm, we found a greater connection between α and Kd when α was computed below 2 m depth (Spearman rank correlation coefficient up to 0.96), and a larger contribution of Kd to α with respect to the beam attenuation coefficient as estimated from lidar measurements and Kd models. Our results suggest that concurrent passive and active optical measurements can be used to estimate total scattering coefficient and backscattering efficiency in waters without optical vertical structure.

15. SUBJECT TERMS
remote sensing, lidar, light attenuation

16. SECURITY CLASSIFICATION OF: a. REPORT	b. ABSTRACT	c. THIS PAGE	17. LIMITATION OF ABSTRACT	18. NUMBER OF PAGES	19a. NAME OF RESPONSIBLE PERSON
Unclassified	Unclassified	Unclassified	UL	10	Richard Gould

19b. TELEPHONE NUMBER *(Include area code)*: 228-688-5587

Relationships between water attenuation coefficients derived from active and passive remote sensing: a case study from two coastal environments

Martin A. Montes,[1,*] James Churnside,[3] Zhongping Lee,[1] Richard Gould,[2] Robert Arnone,[2] and Alan Weidemann[2]

[1]Geosystems Research Institute, Mississippi State University, Mississippi 39529, USA

[2]Naval Research Laboratory, Stennis Space Center, NASA, Mississippi 39529, USA

[3]Earth System Research Laboratory, National Oceanic and Atmospheric Administration, Boulder, Colorado 80305, USA

*Corresponding author: mmontes@gri.msstate.edu

Received 4 January 2011; revised 24 March 2011; accepted 11 April 2011; posted 22 April 2011 (Doc. ID 140476); published 14 June 2011

Relationships between the satellite-derived diffuse attenuation coefficient of downwelling irradiance (K_d) and airborne-based vertical attenuation of lidar volume backscattering (α) were examined in two coastal environments. At 1.1 km resolution and a wavelength of 532 nm, we found a greater connection between α and K_d when α was computed below 2 m depth (Spearman rank correlation coefficient up to 0.96), and a larger contribution of K_d to α with respect to the beam attenuation coefficient as estimated from lidar measurements and K_d models. Our results suggest that concurrent passive and active optical measurements can be used to estimate total scattering coefficient and backscattering efficiency in waters without optical vertical structure.

OCIS codes: 010.4450, 280.0280.

1. Introduction

The diffuse attenuation coefficient of downwelling irradiance (K_d) is a key optical property linked to the variability of underwater light fields in aquatic environments [1]. For this reason, K_d has often been used by modelers to estimate the depth of the euphotic zone (i.e., the depth at which irradiance is 1% of surface value) [2]. Also, K_d has been commonly used to calculate solar heat budgets [3], determine light thresholds for prey–predator relationships [4], estimate coral reef mortality due to thermal stress [5], and indicate water quality status in coastal studies [6].

The magnitude and vertical distribution of K_d are determined by the sunlight geometry and the inherent optical properties of the water [7]. In simple terms, K_d is directly related to the total (water+particulates) scattering (b) and absorption coefficient (a), and inversely related to the average cosine of the zenith angle of refracted solar photons (direct beam) just beneath the sea surface (μ_0) (Table 1). Far from the sea surface, the K_d distribution is mainly driven by variations on the absorption coefficient [8]. Attenuation of the lidar volume backscattering with depth (α) is fully or partially linked to K_d, depending on the lidar spot size at the sea surface ($R = H\theta_{\text{receiver}}$, where H is the lidar carrier altitude above the sea surface and θ_{receiver} is the receiver's field of view) and the beam attenuation coefficient ($c = a + b$) [8]. Assuming a vertically homogeneous distribution of inherent optical properties, when $cR \ll 1$, the exponential decrease of lidar volume backscattering (S) with depth is principally explained by single scattering and $\alpha \to c$ [9]:

0003-6935/11/182990-10$15.00/0

Table 1. List of Acronyms

Symbol	Definition	Units
K_d	diffuse attenuation coefficient of downwelling irradiance	m^{-1}
a	absorption coefficient	m^{-1}
b	scattering coefficient	m^{-1}
c	beam attenuation coefficient	m^{-1}
μ_0	average cosine of solar zenith angle beneath the sea surface	rad
θ_z	solar zenith angle	rad
α	lidar attenuation coefficient	m^{-1}
R	lidar spot size at the sea surface	m rad
H	lidar carrier altitude above the sea surface	m
$\theta_{receiver}$	receiver's field of view	rad
S	lidar volume backscattering	$m^{-1}\,sr^{-1}$
Q	lidar pulse energy	mJ
A_{rcv}	area of the receiver	m
T_{atm}	transmission of the atmosphere	dimensionless
T_{aw}	transmission of the air/water interface	dimensionless
$\beta(\pi)$	lidar volume backscattering at 180°	$m^{-1}\,sr^{-1}$
ζ	lidar range	m
v	speed of light in the vacuum	$m\,s^{-1}$
m	refractive index of seawater	dimensionless
b_b	backscattering coefficient	m^{-1}
$\tilde{b}_b$	backscattering efficiency	dimensionless
R_{rs}	remote sensing reflectance	sr^{-1}
$Z_{(0.01Ed(0+))}$	depth at which downwelling irradiance is 1% of surface value	m
$\bar{\mu}_S$	average cosine of scattering	dimensionless
θ_s	scattering angle	rad
$\beta(\bar{\theta}_S)$	scattering phase function	dimensionless

$$S(\zeta) \approx QA_{rcv}T_{atm}^2T_{aw}^2\beta(\pi)[(v/m)/(2m^2(H + \zeta/m)^2]\exp(-2\zeta(a+b)), \tag{1}$$

where ζ is the lidar range, Q is the pulse energy, A_{rcv} is the area of the receiver, T_{atm} and T_{aw} are the transmission of the atmosphere and the air/water interface, respectively, $\beta(\pi)$ is the volume backscattering evaluated at a scattering angle of 180°, v is the speed of light in vacuum, and m is the refractive index of seawater. Conversely, when $cR \gg 1$, multiple scattering dominates the received signal, and Eq. (1) is no longer a good approximation due to the effects of volume scattering function shape (i.e., forward versus backward directions) and variations associated with the transmitter beam width. In this case, $\alpha \to K_d$, and the lidar volume backscattering can be modeled according to the following expression [9]:

$$S(\zeta) \approx QA_{rcv}T_{atm}^2T_{aw}^2\beta(\pi)[(v/m)(2m^2(H+\zeta/m)^2] \times \exp(-2\zeta\alpha), \tag{2}$$

$$\exp(-\zeta\alpha) \approx \exp(-\zeta(a+b)) + \exp(-a\zeta)(1-\exp(-b\zeta)) /(1+a\sigma^2(v/m)/\mu), \tag{3}$$

where μ and σ^2 are the mean and variance of the Gamma probability density function of photons as a function of lidar range and time. The cR value corresponding to the transition between the "single-backscattering" and "multiple-forward- scattering" regimes is still in debate due to differences between lidar models [8,9]. One way to study the cR threshold for a specific lidar system is to compare simultaneous α values with field measurements of inherent optical properties [10]. This method works when lidar and optical passive observations are concurrent, and have associated a minimum measurement error due to instrument self-shading effects.

Unlike K_d, optical properties influenced by forward scattering of photons (e.g., c, volume scattering function, and backscattering efficiency [i.e., $\tilde{b}_b = b_b/b$, where b_b is the total (water + particulates) backscattering coefficient] are difficult or impossible to study based on remote sensing reflectance (R_{rs}) signatures [11]. For this reason, most of studies reporting b, $\tilde{b}_b$, and c distributions in surface oceanic and coastal waters rely on more accurate methods based on *in-water* determinations [12,13]. Although relatively accurate (~15%) [14,15], retrievals of K_d, a, and b_b based on spaceborne or airborne passive sensors are not vertically resolved, thus they represent integrated values within the first optical depth. This depth restriction is alleviated when active optical systems, such as lidars, are used instead. However, K_d values computed from lidar volume backscattering profiles are commonly quantified with fewer wavelengths with respect to those K_d values derived from R_{rs} measurements obtained with passive optical systems. Another difference to emphasize is that α is not necessarily equivalent to K_d due to the variable contribution of forward scattering at the lidar receiver. Therefore, for a specific light wavelength, α provides additional information

relative to K_d that can be exploited in combination with passive measurements to extract c, b, and $\tilde{b}_b$.

The aim of this study is to investigate how α values derived from an airborne backscattering-based lidar (i.e., the National Oceanic and Atmospheric Administration's Fish Lidar Oceanic Experimental system) relate to K_d values computed from spaceborne R_{rs} measurements having a moderate spatial resolution ($\sim$1.1 km) (Objective 1), and to apply these measurements to estimate b, $\tilde{b}_b$, and c within the first optical depth of two coastal areas (Oregon/Washington and the Afgonak/Kodiak Shelves) characterized by waters having different optical composition (Objective 2). Because of the field of view of our lidar receiver and the relatively high turbidity of the waters under investigation, we hypothesize a substantial correlation between satellite-derived K_d and lidar-based measurements of α.

2. Experiments

A. Study Areas and Sampling Design

Comparisons between airborne lidar and spaceborne passive optical measurements were performed in the eastern shelf of Afgonak/Kodiak Islands (57.68°–58.03 °N, 152.04°–151.26 °W) on 17 August 2002, and in the western shelf off the Oregon/Washington coast (124.11°–124.77 °W 46.16°–46.17 °N) on 24 August 2005 (Fig. 1). In the northern part of the Gulf of Alaska, the aerial transect (hereafter AK1) encompassed a total distance of 40 km and covered shelf locations having relatively high concentration of chromophoric dissolved organic matter as inferred from R_{rs} ratios [16]. The Oregon/Washington aerial transect (hereafter OR1) was longer (48 km) and was conducted perpendicular to the coast and along the west–east direction. Water properties in this study area are determined not only by phytoplankton but also by sediments and colored dissolved matter derived from freshwater plumes associated with the Columbia River. In general, large vertical differences on seawater density (up to 0.22 kg/m) reflected a substantial stratification of the water column during our aerial surveys. AK1 and OR1 locations were selectively chosen based on the following criteria: (1) no flight turns, (2) flight track along the main orientation of phytoplankton or bathymetric gradients, and (3) locations overlapping satellite pixels with minimum solar glint. Given the influence of flying altitude on lidar footprint and signal attenuation with depth, flight missions were always conducted at a constant height of 300 m.

B. Datasets

1. *Active Optical Airborne Measurements*

The laser system used in this study was a nonscanning, radiometric lidar [17] with three major components: (1) the laser and beam-control optics, (2) the receiver optics and detector, and (3) the data collection and display computer. The system also provides information about aircraft position and attitude. The laser was a frequency-doubled, Q-switched Nd:YAG laser that produced 120 mJ of green (532 nm) light in a 12 ns pulse at a rate of 30 pulses per second. The lidar was nearly normal to the sea surface (15° off nadir), with a beam divergence and receiver field of view of 17 mrad. Signal arriving at the receiver was polarized in the perpendicular direction. Lidar backscattering measurements in each study area were collected between 1 and 3:30 p.m. to maximize temporal matchup with spaceborne imagery obtained by the Moderate Resolution Imaging Spectroradiometer (MODIS) sensor onboard the Aqua satellite. The time difference between lidar and MODIS measurements never exceeded 25 min.

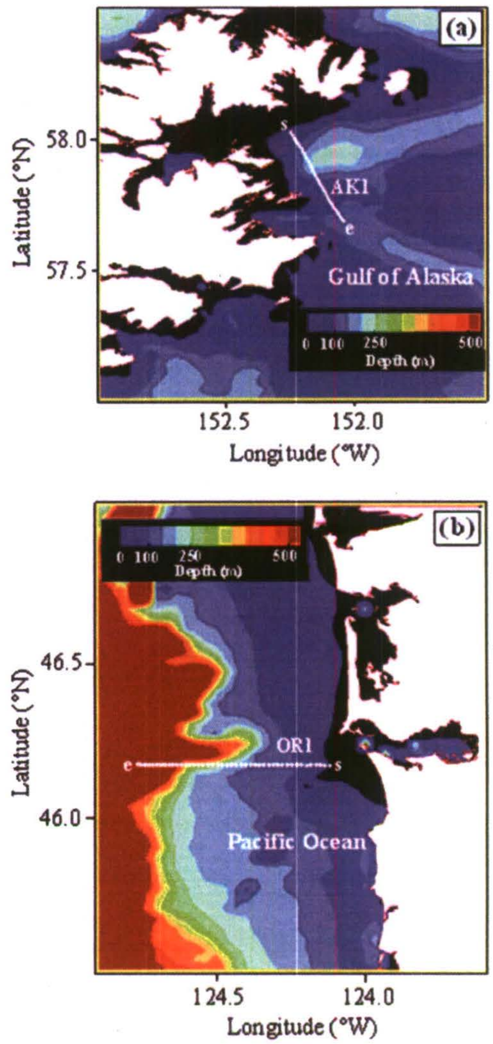

Fig. 1. (Color online) Geographic location of lidar surveys. (a) Eastern shelf of Afgonak/Kodiak Islands, (b) Western shelf off the Oregon/Washington coast. AK1 and OR1 are the airborne transects matching 1.1 km satellite ocean color data (white dots), land (white), and bathymetry with 1/30 deg resolution (color contours), missing data (black areas). Flight direction is indicated based on initial (s) and final (e) sampling locations.

2. Passive Optical Spaceborne Measurements

MODIS–Aqua images (local area coverage, Level 2 OC, 1.1 km footprint) were obtained from NASA (http://oceancolor.gsfc.nasa.gov/). Geo-located, calibrated, and atmospheric corrected R_{rs} values were obtained for spectral bands 9 (438–448 nm), 10 (483–493 nm), 11 (526–536 nm), 12 (546–556 nm), and 13 (662–672 nm), and used to derive inherent optical properties (see Subsection 2.C.1). Unlike other ocean color sensors with intermediate spatial resolution (e.g., SeaWiFS), MODIS has a radiometric channel dedicated to ocean applications centered at 531 nm (i.e., band 11) and spectrally close to the laser wavelength used in this study. Also, detection limits of MODIS are relatively low (e.g., signal/noise at 490 nm~ twofold) with respect to other sensors.

3. Ancillary Information

Wind speed and direction during the AK1 and OR1 surveys were obtained from meteorological stations located at the Kodiak Island and Aberdeen airports, respectively (http://www.wunderground.com/). Receiver`s radiance contributions due to foam, glint, and bubbles are highly dependent on wind field characteristics [18] Therefore, wind information is critical to quantify these nonwater radiance contributions and obtain accurate estimates of remotely sensed optical properties.

C. Processing of Remote Sensing Data

1. Satellite Remote Sensing Reflectance

The operational atmospheric correction for ocean color products suggested by NASA is based on the Gordon and Wang algorithm [19]. The performance of this model may be compromised in coastal waters like those investigated here. This issue was examined in our study areas by using the L2 OC flag 12 or "TURBIDW." MODIS-derived total absorption and backscattering coefficients at 532 nm were computed based on R_{rs} values at five wavelengths using a new version of the quasi-analytical inversion model of Lee *et al.* [20]. Seawater backscattering and absorption coefficients were obtained from Smith and Baker tables [21]. The uncertainty of $a(532)$ and $b_b(532)$ estimates using this quasi-analytical parameterization is about $\pm 10\%$ [15]. $K_d(532)$ values were computed by two methods.

Method I [22]:

$$K_d(532) \cong [a(532) + b_b(532)]/\mu_0, \tag{4}$$

Method II [14]:

$$K_d(532) \cong m_0 a(532) + m_1 b_b(532) \times (1 - m_2 \exp(-m_3 a(532)), \tag{5}$$

where m_0, m_1, m_2, and m_3 are parameters that vary with solar zenith angle and depth interval used to estimate K_d. Unlike Eq. (4), K_d estimates with Method II are calculated with a semiempirical parameterization derived from radiative transfer theory [14].

2. Airborne Lidar Backscattering

Raw lidar data in volts were converted to photocathode current values based on the specific gain of the photomultiplier. Afterward, the depth of each lidar sample was found using the surface return as a reference, and the return was multiplied by a calibration factor to convert photocathode current to lidar volume backscattering measurements in $m^{-1}\,sr^{-1}$. The calibration factor involves several parameters related to geometry (e.g., sampling altitude) and lidar system characteristics (e.g., pulse energy, area of receiver).

Calculation of α was performed for each lidar shot, followed by screening and removal of shots containing subsurface scattering layers [23]. The last step was necessary to remove the influence of vertical structure on K_d and α comparisons. For each lidar waveform, α was computed by linear regression as the slope between water depth (independent variable) and $\ln(S)$ (dependent variable). This analysis was performed using full resolution profiles (i.e., every 0.1 m, accuracy = 0.001 m) over different depth ranges (0–1, 0–5, 0–10, 0–15, 0–20, 2–5, 2–10, 2–15, and 2–20 m) to evaluate the influence of surface effects (e.g., bubbles, waves) on $K_d - \alpha$ correlations and find the optimum vertical interval to match the penetration depth of passive sensors (i.e., $1/K_d$). Lidar probing depth was estimated as the depth at which lidar volume backscattering first fell below the level of the background light plus 10 standard deviations of the noise [23]. Last, we related differences between $K_d(532)$ derived from MODIS at 1.1 km resolution with the median, and different averages (arithmetic, geometric, and harmonic) of α value within the satellite footprint. This numerical exercise was intended to examine potential changes of averaged α at 1.1 km due to statistical distribution changes.

3. Modeling of b, b_b/b, and c

In marine waters with b_b/a up to ~0.25, the diffuse attenuation coefficient of downward irradiance can be accurately (i.e., ~5% relative error) approximated using a, b, and the solar altitude [7]:

$$K_d \cong \mu_0^{-1}(a^2 + G(\mu_0)ab)^{0.5}, \tag{6}$$

$$G(\mu_0) = 0.425\mu_0 \_ 0.19 \quad \text{for } 0 \le z \le z_{(0.01\mathrm{Ed}(0+))}, \tag{7}$$

where G is a coefficient determining the relative contribution of scattering to vertical diffuse attenuation of irradiance and is defined for a water depth (z) interval coinciding with the euphotic zone, i.e., z at which surface downwelling irradiance [Ed(0+)] is

reduced in 99%. Note that Eq. (7) (hereafter G1) was developed from measurements made in San Diego Harbor with a very narrow spectrum of b-normalized volume scattering function or scattering phase function [24]. Based on a more realistic set of Monte Carlo simulations using 12 different scattering phase functions and a broader range of b_b/a (0.4–2.6) values, a new approximation for G was found (hereafter G2) [1]. Unlike G1, this model is influenced not only by geometry of surface illumination but also by underwater light field distribution:

$$G(\mu_0, \tilde{\mu}_S) = \mu_0(2.636/\tilde{\mu}_S - 2.447) - (0.849/\tilde{\mu}_s - 0.739), \tag{8}$$

$$\tilde{\mu}_S = 0.5\int_0^{\pi} \beta(\tilde{\theta}_S)\cos\theta_S \sin\theta_S \mathrm{d}\theta_S, \tag{9}$$

where θ_s is the scattering angle in radians and $\tilde{\mu}_S$ is the average cosine of single scattering events in all directions. In other words, $\tilde{\mu}_S$ is a parameter related to the "shape" of the volume scattering function and can be empirically linked to the backscattering efficiency [25]:

$$\tilde{\mu}_S = (1 - 4\tilde{b}_b^2)/(1.0144 + 2.6307\tilde{b}_b) - 1.2772\tilde{b}_b^2), \quad r^2 > 0.82, \quad 0.0022 < \tilde{b}_b < 0.146. \tag{10}$$

This relationship is spectrally independent and was developed with 869 comparisons between volume scattering functions and inherent optical properties encompassing a broad range of optical water types, and having b varying between 0.008 and $10\,\mathrm{m}^{-1}$. Assuming that $\alpha \cong K_d$ and given that $b = b_b/\tilde{b}_b$ with b_b estimated from inversion modeling [20], we can create synthetic b's from $\tilde{b}_b$ values. The iterative numeric procedure converges when the right part of Eq. (6) is within $\pm 10\%$ of α. This approach was applied to different G functions [Eqs. (7) and (8)], and resulting $b(532)$ estimates were later added to $a(532)$ values computed from inversion modeling [20] in order to calculate $c(532)$.

D. Statistical Analysis

The relationship between α and MODIS-derived $K_d(532)$ measurements at 1.1 km resolution was quantified using nonparametric Spearman rank correlation coefficients (ρ_s). The relative importance of size distribution and composition of particulates on $\tilde{b}_b$ variability was estimated by calculating ρ_s between $\tilde{b}_b$ and two R_{rs} ratios ($\mathrm{R1} = R_{rs}(443)/R_{rs}(488)$ [26], and $\mathrm{R2} = R_{rs}(667)/R_{rs}(551)$) that are sensitive to variations on particle size distribution. Unlike R1, R2 is based on a particle size distribution proxy developed with SeaWiFS spectral channels [27]. Relationships among $\tilde{b}_b$, R1, and R2 were examined using *in situ* measurements obtained from surface waters (i.e., 0.6 m depth) adjacent to Scripps Institution of Oceanography (University of California San Diego). R_{rs} was calculated from upwelling radiance below the sea surface and downwelling irradiance above the sea surface measurements obtained with a Hyperspectral (wavelength = 400–800 nm, spectral resolution = 1 nm) Tethered Spectral Radiometer Buoy (Satlantic Inc.) [28]. Particle size distribution spectra were characterized with a Coulter Counter Multisizer III (Beckman Coulter, size range = 2–60 μm) and a laser diffractometer LISST-100x (Sequoia Scientific Inc., size range = 1–200 μm). We quantified the response of R1 and R2 as a function of the particle size distribution slope (M) estimated from Multisizer III (γ) and LISST (χ) using linear regression [$\ln(N(D)) = M\ln(D) + I$, where N is the number of particles per bin and unit of volume in cubic meters, D is the diameter range in meters, and I is the intercept of the regression curve].

3. Results

A. Comparisons Between α and K_d

Relative absorption versus backscattering of photons, as reflected by $a(532)/b_b(532)$ ratios, varied between AK1 (range, 0.040–0.052; median, 0.046) and OR1 (range, 0.035–0.091; median, 0.057) surveys; however, these differences did not have a clear impact on absolute $|\alpha - K_d(532)|$ values computed at 1.1 km resolution and based on a lidar depth interval having a maximum ρ_s between α and $K_d(532)$ as derived from Method I (Table 2). In general, depth intervals with the highest correlation coefficients were computed at depths <5 m and were larger (ρ_s increases up to 19.7% in OR1 and 14.3% in AK1) when α was calculated below the first 2 m of the water column. Also, a consistent observation at all depth intervals under investigation was the greater correlation between α and $K_d(532)^{\text{Method I}}$ in OR1 with respect to AK1 surveys.

The larger $\alpha - K_d(532)^{\text{Method I}}$ correlation coefficient in OR1 corresponded with a larger penetration depth of the lidar signal and a larger first optical depth (i.e., $1/K_d(532)^{\text{Method I}}$) as derived from ocean color data. In this area, the lidar penetration depth averaged 34.4 m, based on a noise threshold between 5 and $15 \times 10^{-8}\,\mathrm{sr}^{-1}\,\mathrm{m}^{-1}$. The penetration depth varied from 12 m near the coast to 60 m in those westernmost locations characterized by more oceanic waters. The inverse of $K_d(532)^{\text{Method I}}$ averaged 7.3 m, and varied between 2.5 and 14.3 m from the coast to the west. The highest $\rho_s(\alpha - K_d(532)^{\text{Method I}})$ was obtained over depth intervals of 0–10 and 2–10 m when all locations (number of observations *observations* = $n = 44$) were part of the analysis. We also considered a reduced dataset (i.e., $n = 16$) that included only data ≥30 km from the coast where there was minimal terrigenous material. These data had the greatest correlation at greater depths ($\rho_s = 0.89$ for 0–20 and 2–20 m). However, for a subsequent interpretation of $\alpha - K_d(532)^{\text{Method II}}$ relationships and the horizontal variability of α along

Table 2. Correlation Between Passive and Active Optical Properties in Oregon/Washington and Alaskan Coastal Waters[a]

Experiment	Depth Range (m)	$a(532)$	$b_b(532)$	$K_d(532)^{\text{Method I}}$
OR1	0–1	−0.70 (10^{-7})	−0.88 (10^{-7})	−0.70 (10^{-7})
	0–5	0.79 (10^{-7})	0.63 (10^{-6})	0.79 (10^{-7})
	0–10	0.96 (10^{-7})	0.87 (10^{-7})	**0.96 (10^{-7})**
	0–10[b]	0.87 (10^{-7})	0.90 (10^{-7})	0.87 (10^{-7})
	0–15[b]	0.87 (10^{-7})	0.87 (10^{-7})	0.87 (10^{-7})
	0–20[b]	0.89 (10^{-7})	0.90 (10^{-7})	0.89 (10^{-7})
	2–5	0.94 (10^{-7})	0.83 (10^{-7})	0.94 (10^{-7})
	2–10	0.96 (10^{-7})	0.87 (10^{-7})	**0.96 (10^{-7})**
	2–10[b]	0.86 (10^{-7})	0.88 (10^{-7})	0.86 (10^{-7})
	2–15[b]	0.87 (10^{-7})	0.87 (10^{-7})	0.87 (10^{-7})
	2–20[b]	0.89 (10^{-7})	0.90 (10^{-7})	0.89 (10^{-7})
AK1	0–1	−0.64 (9 10^{-5})	−0.673 (4 10^{-5})	−0.662 (2 10^{-5})
	0–5	2.8 10^{-3} $(0.99)^{\text{ns}}$	0.025 $(0.859)^{\text{ns}}$	−3.6 10^{-3} $(0.998)^{\text{ns}}$
	0–10	0.64 (2 10^{-5})	0.700 (2 10^{-5})	0.642 (3 10^{-5})
	0–15	0.74 (2 10^{-5})	0.745 (2 10^{-5})	0.736 (2 10^{-7})
	0–20	0.70 (2 10^{-5})	0.706 (2 10^{-3})	0.710 (2 10^{-7})
	2–5	0.64 (2 10^{-5})	0.664 (6 10^{-6})	0.649 (2 10^{-5})
	2–10	0.73 (2 10^{-7})	0.771 (2 10^{-7})	0.734 (2 10^{-7})
	2–15	0.76 (2 10^{-7})	0.756 (2 10^{-7})	**0.757 (2 10^{-7})**
	2–20	0.70 (2 10^{-7})	0.703 (2 10^{-7})	0.704 (2 10^{-7})

[a]For each correlation, probability of accepting the null hypothesis (H_o, $\rho_s = 0$; i.e., variables are uncorrelated) is indicated between parentheses. Nonsignificant correlations at 95% (ns) confidence level, highest $\alpha - K_d(532)^{\text{Method I}}$ correlations are highlighted in bold. OR1 and AK1 are defined in Subsection 2.A.

[b]Calculated with measurements obtained at ≥30 km distance with respect to the starting flying point.

each transect, we used α calculated between 2 and 10 m to provide more comparisons and representative samples of the whole survey. In AK1, the penetration depth of the lidar averaged 20 m for a noise threshold between 3 and $11 \times 10^{-10}\ \text{sr}^{-1}\ \text{m}^{-1}$. The optical depth was generally shallower ($\tilde{x} = 5.9$ m) and less variable (4.1–7.5 m) than at OR1. The maximum $\rho_s(\alpha - K_d(532)^{\text{Method II}})$ was obtained for α values computed using a 2–15 m depth interval ($\rho_s = 0.757$, $n = 36$).

The similarity between $K_d(532)$ and α computed below 2 m depth was corroborated based on comparisons between α and $K_d^{\text{Method II}}$ (Table 3). Since the Method II algorithm only resolves $K_d(532)$ at three sunlight geometries, $K_d^{\text{Method II}}$ values were calculated between two solar zenith angles (i.e., 60° and 30°) in order to include all possible solar elevations during the airborne campaigns (i.e., 42° to 48°). As expected, absolute differences between the magnitude of α computed at the maximum $\rho_s(\alpha - K_d(532)^{\text{Method I}})$ and $K_d(532)^{\text{Method II}}$ tended to be minimum for larger depth ranges. In OR1, the satellite overpass on 24 August 2005 was relatively early (i.e., local time = 13:05 h) and the root mean square error (RMS) between lidar and passive attenuation coefficients was smaller when the Sun was close to the vertical (i.e., Method I simulations at 30°). Conversely, MODIS–Aqua R_{rs} measurements during lidar surveys of 17 August 2002 were obtained late in the afternoon (local time = 15:05 h), resulting in a closer agreement between α and $K_d(532)^{\text{Method II}}$ at the two solar positions (e.g., RMS = 0.022, depth range = 0–20 m, zenith angle 30° and 60°).

Overall, α values at the optimum correlation depth range were closer to $K_d(532)^{\text{Method II}}$ than $K_d(532)^{\text{Method I}}$. The relative biases {i.e., $[(\alpha - K_d(532))/K_d(532)]$} as percentages were +9.3% (Method II) and +11.3% (Method I) in OR1, and +8.7% (Method II) and +8.9% (Method I) in AK1. These biases were much greater than K_d differences (<2%) associated to changes on solar altitude during each aerial survey (~0.03%). Also, statistical variations of α within the satellite footprint had a minor impact on observed $K_d(532) - \alpha$ differences since the magnitude of different α averages (i.e., arithmetic, geometric, harmonic) and median only differ in the fourth decimal unit.

The light interaction mechanism explaining the aforementioned $\alpha - K_d(532)^{\text{Method I}}$ correlations differed between study areas. In OR1, the lidar attenua-

Table 3. Difference Between α and $K_d(532)^{\text{Method II}}$ for Two Different Solar Zenith Angles[a]

Experiment	Depth Range (m)	$\theta_z = 0.5235$	$\theta_z = 1.0471$
OR1	0–1	0.040 (17.9)	0.048 (12.2)
	0–5	0.038 (15.5)	0.049 (12.4)
	0–10	0.037 (13.5)	0.049 (12.4)
	0–20[b]	0.008 (12.0)	0.012 (6.8)
AK1	0–1	0.029 (16.3)	0.021 (9.1)
	0–5	0.025 (13.8)	0.022 (9.4)
	0–10	0.022 (11.3)	0.023 (9.5)
	0–20	0.022 (11.4)	0.022 (9.3)

[a]Each value corresponds to root mean square between the arithmetic average of α at the respective depth interval (i.e., OR1, 2–10 m; AK1, 2–15 m) and MODIS-derived $K_d(532)$ computed at each 1.1 km pixel. Between parentheses is the relative difference as percentage; i.e., 100 $[(\alpha - K_d(532)^{\text{Method II}})/K_d(532)^{\text{Method II}}]$.

[b]Idem to Table 2.

tion below 2 m depth was primarily driven by $a(532)$ changes. Conversely, in AK1, the effects of $a(532)$ and $b_b(532)$ on α were comparable. This finding is better illustrated in Fig. 2, where we evaluated the horizontal coherence between satellite-based $K_d(532)^{\mathrm{Method\ I}}$ and airborne-based α for spatial scales between 1 and 50 km. For this analysis, we used Method I rather than Method II to derive $K_d(532)$ because Method I depends on μ_0, while Method II estimates are constrained by solar position.

In OR1, $K_d(532)^{\mathrm{Method\ I}}$, $a(532)$, and α decreased by 80% from the coast to offshore locations [Fig. 2(a)]. On the other hand, $b_b(532)$ was relatively low ($<0.015\ \mathrm{m}^{-1}$) within the first 6 km of the lidar survey, reached a maximum (up to $0.018\ \mathrm{m}^{-1}$) at intermediate distances from shore (9 to 21 km), and decreased to minimum values ($<0.005\ \mathrm{m}^{-1}$) by the offshore end of the transect. Not surprisingly, satellite-derived $K_d(532)^{\mathrm{Method\ I}}$ estimates had a larger uncertainty ($\pm 20\%$) than averaged α values ($\pm 5\%$ in average, n per pixel $= 200$) within the same 1.1 km footprint. Despite these similarities, there were some sections along the transect (e.g., 24 to 29 km) where $K_d(532)^{\mathrm{Method\ I}}$ error bars did not overlap the arithmetic mean of lidar attenuation coefficient values. Like the OR1 results, the spatial patterns of $K_d(532)^{\mathrm{Method\ I}}$ and α in AK1 had a positive covariation, and α was always greater than $K_d(532)^{\mathrm{Method\ I}}$ [Fig. 2(b)]. However, there were striking differences in terms of how the inherent optical properties affected K_d. Indeed, $b_b(532)$ values in the Alaskan Shelf covaried with $K_d(532)^{\mathrm{Method\ I}}$, $a(532)$ and α, and were related to variations in the bathymetry (i.e., 50–70 m depth over shallow "banks" versus 150–250 m over the "troughs"). The presence of "banks" (e.g., 18–22 km from the start) and "troughs" (e.g., 10–12 km) were consistently discriminated by MODIS–Aqua and lidar measurements as areas characterized by relatively high ($1/\alpha = 5.7$–6.0 m, $1/K_d(532)^{\mathrm{Method\ I}} = 6.0$–$7.7$ m) and low ($1/\alpha = 4.2$–4.5 m, $1/K_d(532)^{\mathrm{Method\ I}} = 4.2$–$4.8$ m) water visibility values, respectively.

B. Analysis of Inherent Optical Properties Computed from α and K_d

Assuming that α is not different from K_d, we can use Eq. (6) to model $\tilde{b}_b$ and subsequently b and c based on active and passive optical properties. The approximation $\alpha \cong K_d$ was met by selecting a subset of values in each transect having the minimum $|\alpha - K_d|$ magnitude. Under this premise, we extracted four groups from Fig. 2: "coastal" (locations 5, 9, and 11 km) and "oceanic" (32, 44, and 46 km) in OR1, and "banks" (2, 4, and 22 km) and "troughs" (9, 10, and 30 km) in AK1. Errors in calculating $b(532)$, $\tilde{b}_b(532)$, and $c(532)$ from Eq. (6) with G1 and G2 were 24%, 26%, 38%, and 77%, 79%, 83%, respectively. In general, higher $b(532)$ (up to $0.81\ \mathrm{m}^{-1}$) and $c(532)$ (up to $1.09\ \mathrm{m}^{-1}$), and lower $\tilde{b}_b(532)$ (up to 0.015) values

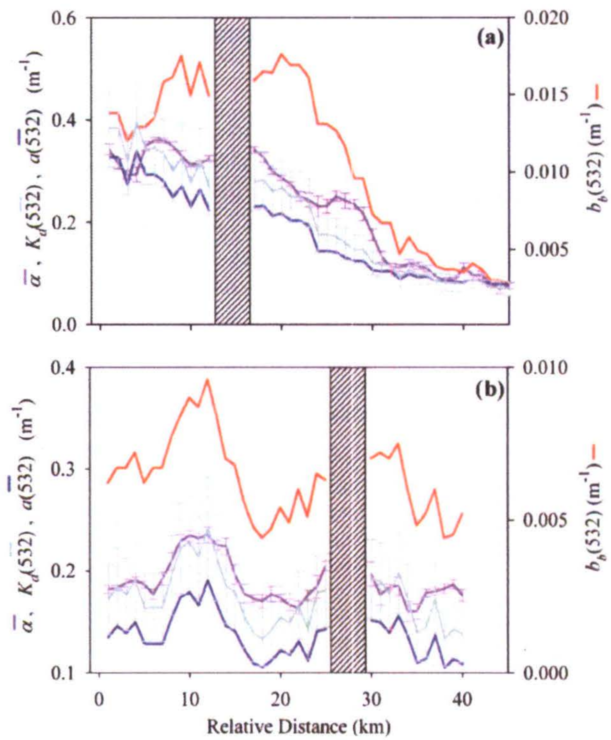

Fig. 2. (Color online) Spatial coherence between satellite-derived $K_d(532)^{\mathrm{Method\ I}}$ and airborne-based α. (a) OR1; (b) AK1. For each comparison, α is the arithmetic mean within the satellite footprint (pink solid curve, left axis), $a(532)$ (blue solid curve, left axis), $K_d(532)^{\mathrm{Method\ I}}$ (gray solid curve, left axis), and $b_b(532)$ (red solid curve, right axis), missing lidar data (hatched bars). To better illustrate $K_d(532)^{\mathrm{Method\ I}} - \alpha$ differences, error bars of $a(532)$ and $b_b(532)$ are not shown.

Table 4. Summary of Inherent Optical Properties Estimated from α and Eqs. (6)–(8)[a]

Experiment			G1 $b(532)$	G1 $\tilde{b}_b(532)$	G1 $c(532)$	G2 $b(532)$	G2 $\tilde{b}_b(532)$	G2 $c(532)$
OR1	Coastal	Min	0.494	0.020	0.747	0.272	0.015	0.524
		Max	0.607	0.033	0.877	0.813	0.060	1.089
	Oceanic	Min	0.016	0.031	0.074	0.020	0.040	0.077
		Max	0.173	0.120	0.265	0.074	0.100	0.166
AK1	Banks	Min	0.236	0.023	0.367	0.040	0.002	0.17
		Max	0.320	0.025	0.469	4.091	0.146	3.42
	Troughs	Min	0.120	0.018	0.256	0.026	0.002	0.19
		Max	0.466	0.024	0.645	3.273	0.120	4.37

[a]Range of values for each estimate based on one (i.e., G1) or many (i.e., G2) water types.

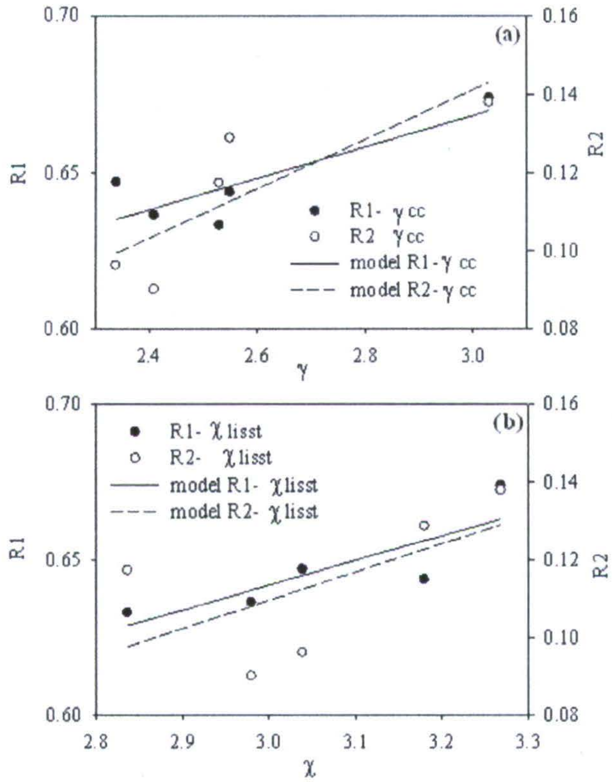

Fig. 3. Response of remote sensing reflectance ratios to variability of particle size distribution. R1, $R_{rs}(443)R_{rs}(488)$ (left axis) and R2, $R_{rs}(670)/R_{rs}(555)$ (right axis) are plotted as functions of particle size spectrum slope derived from Coulter counter (a) Multisizer III (γ) and (b) LISST (χ).

were estimated in OR1 than in AK1 (Table 4). In OR1, the "coastal" group was characterized by higher $b(532)$ (up to tenfold) and $c(532)$ (up to sevenfold) and lower $\tilde{b}_b(532)$ (up to 0.4-fold) values than those for the "oceanic" group. Shallower waters of AK1 associated with submarine banks had typically lower $b(532)$ (up to $0.24\,\mathrm{m}^{-1}$) and $c(532)$ (up to $0.37\,\mathrm{m}^{-1}$) and higher $\tilde{b}_b(532)$ (up to 0.025) values than those over deep canyons (i.e., "troughs").

The concurrent use of active and optical passive measurements in this study was also applied to estimate second-order optical attributes affecting

Table 5. Statistical Relationships Between Particle Size Distribution and R_{rs} Ratio Variability[a]

		M	I	n	r^2
R1	γ	0.050 (0.018)*	0.518 (0.048)*	5	0.712
	χ	0.080 (0.030)*	0.403 (0.091)*	5	0.704
R2	γ	0.063 (0.024)*	−0.048 (0.062)	5	0.692
	χ	0.073 (0.056)	−0.108 (0.172)	5	0.358

[a]The linear model used to estimate slope of particle concentration (y) as a function of particle size range (x) is $y = Mx + I$; M and I are the slope and intercept of the regression curve, respectively. Between parentheses is the standard error of each regression coefficient, M and I are different from 0 at 95% confidence level (*), and n is the number of comparisons. R1, R2, γ, and χ are explained in Subsection 2.D.

Table 6. Influence of Particle Size Distribution on Spatial Variability of $\tilde{b}_b(532)$[a]

Experiment	ρ_s	P	n
OR1	0.60	0.24	6
	0.60	0.24	6
AK1	0.78	0.06	6
	0.87	0.03*	6

[a]ρ_s is the Spearman correlation coefficient, P is the probability of rejecting the null hypothesis (H_o, $\rho_s = 0$) at 95% confidence level (*), and n is the number of comparisons. For each subset, first and second row correspond to $\tilde{b}_b$ estimates using G1 and G2, respectively.

magnitude of $\tilde{b}_b(532)$ in each marine environment. Preliminary results based on data collected in near-shore waters of the Southern California Bight revealed a positive covariation between the slope of particle size distribution estimated from two instruments (Multisizer III and LISST), and two different R_{rs} ratios in the visible range (Fig. 3). Based on linear regression, we found that remote sensing reflectance indices of particle size distribution had a greater covariation with particle size spectra measured by Multisizer III. This relationship was stronger (i.e., higher coefficient of determination, r^2) for comparisons based on $R_{rs}(443)/R_{rs}(488)$ (Table 5). The lower performance of R2 for detecting changes on particle size distribution was even worse (i.e., r^2 up to 14% lower) when R2 was calculated with SeaWiFS spectral channels [i.e., $R_{rs}(670)/R_{rs}(555)$] [27]. Thus, we only examined *a posteriori* correlations between $R_{rs}(443)/R_{rs}(488)$ and $\tilde{b}_b(532)$ values. These simple correlations illustrate the greater effect of particle size distribution changes on $\tilde{b}_b(532)$ variability in AK1 than in OR1, and the greater impact of different particle size ranges on G2-derived inherent optical properties than those derived from G1 in AK1 (Table 6).

4. Discussion

The value of α in oceanographic studies will vary due to the type of lidar system and the turbidity of the water under study. At 1.1 km resolution, concurrent airborne-derived α and satellite-derived K_d in shelf waters of Alaska and Oregon/Washington during summer showed that α during these experiments was a good predictor of K_d in the green spectral range (i.e., wavelength = 532 nm). Indeed, and based on single linear regression models, we found for each survey that α (dependent variable) was related to K_d (independent variable) with a regression slope (AK1, 1.074 ± 0.132 standard error, $n = 36$; OR1, 0.975 ± 0.053, $n = 44$) and intercept (AK1, -0.030 ± 0.025 standard error; OR1, -0.013 ± 0.013) not statistically different from 1 and 0, respectively. The connection between lidar-derived α and K_d was previously reported in the Southern California Bight [10].

Similar to our study, they found that α values at 20 m depth were mainly determined by K_d and not

c (see linear regression slope of Eqs. 5 and 6 in [10]). However, in contrast with our findings, their $\alpha - K_d$ regression slope was below unity. We attribute this apparent discrepancy to differences in cR. In the Southern California Bight study [10], the laser beam divergence angle (43 mrad) and receiver field of view (26 mrad) were larger with respect to our study, and lidar measurements were obtained from the ship deck (i.e., distance between lidar source/detector and sea surface was 10.3 m). Given this geometry, their R ($\sim$0.08 m) and cR ($\sim$0.01) values were relatively small compared with our values ($R \sim 2.5$ m, $cR \sim 1$). Therefore, as cR becomes smaller than 1 (i.e., Churnside *et al.*'s study [10]), c is expected to explain a larger fraction of K_d [29]. Another variable decreasing cR in contribution [10] was their lower $c(532)$ values (mean $= 0.098\,\mathrm{m^{-1}}$) with respect to our study (AK1, $0.173\,\mathrm{m^{-1}}$; OR1, $0.193\,\mathrm{m^{-1}}$). Note that K_d and c determinations by [10] were more accurate than ours since they were derived from in-water measurements. Finally, it is worth emphasizing that our lidar results are based on cross-polarized lidar returns, while the study in [10] describes values for the copolarized returns. Multiple forward scattering can produce a reduced attenuation of the cross-polarized returns under some conditions [30].

Despite the overall agreement between magnitude of α and MODIS-derived $K_d(532)$ measurements during the AK1 and OR1 surveys, we detected substantial changes (up to +0.088 in OR1 and +0.049 in AK1) between these two properties at specific locations along the transects (e.g., 26–28 km in OR1, 18 km in AK1). Since α values lie between c and K_d [8–10] and c is always larger than K_d, it is suggested that the observed increase of α with respect to the $K_d(532)$ magnitude was associated in these locations with a larger relative contribution of $c(532)$ to α, and, consequently, a greater proportion of forward scattering defining the underwater light field. We attribute these spatial changes (i.e., within and between transects) to the presence of different optical water types.

Although averaged hourly wind speed was higher during the OR1 survey ($4.44\,\mathrm{m\,s^{-1}}$) than during the AK1 survey ($3.33\,\mathrm{m\,s^{-1}}$), its influence on $\alpha - K_d(532)$ differences was secondary due to three main reasons. First, and based on other studies [31], the greater wind intensity and associated production of subsurface bubbles in Oregon/Washington is expected to have a minor impact on lidar volume backscattering ($\sim$25%) compared to observed relative changes between α and $K_d(532)$ (up to 60%). Second, our $\alpha - K_d(532)$ comparisons were based on α calculated below 2 m depth, thus eliminating major interference due to "surface" effects. This interference was more pronounced when $K_d(532)$ was estimated with Method I since the Method II approach was developed using constant and relatively weak winds (i.e., $5\,\mathrm{m\,s^{-1}}$). Last, the influence of wind-mediated changes on sea surface slopes (cross and up/down) and subsequent contribution of Sun glint to R_{rs} was ruled out as a possible major bias of $K_d(532)$ estimates since the specific radiance threshold at 865 nm proposed for MODIS–Aqua (i.e., flag MODGLINT or moderate Sun glint contamination) was never exceeded during the analysis of ocean color data.

For a specific range of oceanographic conditions and lidar system parameters, active and passive optical measurements were combined in this study to calculate inherent optical properties related to magnitude and angular distribution of light scattering. Values of $b(532)$, $c(532)$, and $\tilde{b}_b(532)$ can also be estimated by making equal Eqs. (5) and (6) and solving for b. However, this mathematical procedure has some drawbacks. First, the use of two models is adding more error ($\sim$12%) to the final estimates. Second, K_d models based on passive optical measurements are based on b_b/a changes, thus forward scattering contributions are not quantified. The median of $b(532)$ ($n = 3$) in OR1 (G1, $0.49\,\mathrm{m^{-1}}$) and AK1 (G1, $0.36\,\mathrm{m^{-1}}$) as estimated from G1 was within the range of oceanic ($0.275\,\mathrm{m^{-1}}$) and coastal (1.21 to $1.82\,\mathrm{m^{-1}}$) values reported at the same wavelength in Southern California waters [24]. Our G1-based $c(532)$ estimates (median in OR1, $0.55\,\mathrm{m^{-1}}$; AK1. $0.48\,\mathrm{m^{-1}}$) were also intermediate between oligotrophic (e.g., $0.2\,\mathrm{m^{-1}}$) and eutrophic (e.g., up to $10\,\mathrm{m^{-1}}$) marine environments [32]. Unlike $b(532)$ and $c(532)$, our estimates of backscattering probability at 532 nm were sometimes beyond (e.g., oceanic in OR1, G2-based in AK1) the maximum $\tilde{b}_b$ values measured in the Pacific Central Gyre (0.04–0.06) [13] and the Bahamas Shelf during a "whiting event" ($\sim$0.05) [12]. Given the relative low signal in our oceanic locations and the high uncertainty (relative error up to 79%) of $\tilde{b}_b(532)$ estimates using more realistic volume scattering functions (i.e., G2), we suggest that observed variations of $\tilde{b}_b(532)$ with respect to literature values were apparent. The use of multiple and different optical signals in this research allowed us not only to quantify a budget of inherent optical properties but also to investigate additional physical aspects related to $\tilde{b}_b$ behavior due to variations on particle size distribution. In that regard, the substantial and exclusive correlation found between G2-based $\tilde{b}_b$ and $R_{rs}(443)/R_{rs}(488)$ in AK1 is indirectly suggesting two important facts: the more heterogeneous nature of the volume scattering function in AK1 with respect to OR1, and the greater importance of other factors (e.g., changes on particle composition due to river sediments) affecting backscattering efficiency during OR1 surveys.

This work was supported by the Naval Research Laboratory (NRL) internal project "3D Remote Sensing with a Multiple-Band Active and Passive System: Theoretical Basis," PBE0601153N.

References

1. J. T. O. Kirk, "Volume scattering function, average cosines, and the underwater light field," Limnol. Oceanogr. **36**, 455–467 (1991).

2. Z. Lee, A. Weidemann, J. Kindle, R. Arnone, K. Carder, and C. Davis, "Euphotic zone depth: its derivation and implication to ocean-color remote sensing," J. Geophys. Res. **112**, C03009 (2007).
3. M. R. Lewis, M. E. Carr, G. C. Feldman, E. Wayne, and C. McClain, "Influence of penetrating solar radiation on the heat budget of the equatorial Pacific Ocean," Nature **347**, 543–545 (1990).
4. Ø. Varpe and Ø. Fiksen, "Seasonal plankton-fish interactions: light regime, prey phenology, and herring foraging," Ecology **91**, 311–318 (2010).
5. R. P. Dunne and B. E. Brown, "Penetration of solar UVB radiation in shallow tropical waters and its potential biological effects on coral reefs; results from the central Indian Ocean and Andaman Sea," Mar. Ecol. Prog. Ser. **144**, 109–118 (1996).
6. M. A. Montes-Hugo, S. Alvarez-Borego, and A. Giles-Guzmán, "Horizontal sighting range and Sechii depth as estimators of underwater PAR attenuation in a coastal lagoon," Estuaries **26**, 1302–1309 (2003).
7. J. T. O. Kirk, "Dependence of relationship between inherent and apparent optical properties of water and solar altitude," Limnol. Oceanogr. **29**, 350–356 (1984).
8. H. R. Gordon, "Interpretation of airborne oceanic lidar: effects of multiple scattering," Appl. Opt. **21**, 2996–3001 (1982).
9. R. E. Walker and J. W. McLean, "Lidar equations for turbid media with pulse stretching," Appl. Opt. **38**, 2384–2397 (1999).
10. J. H. Churnside, V. T. Viatcheslav, and J. J. Wilson, "Oceanographic lidar attenuation coefficients and signal fluctuations measured from a ship in the Southern California Bight," Appl. Opt. **37**, 3105–3111 (1998).
11. H. R. Gordon, "Sensitivity of radiative transfer to small-angle scattering in the ocean: quantitative assessment," Appl. Opt. **32**, 7505–7511 (1993).
12. H. M. Dierssen, R. C. Zimmerman, and D. J. Burdige, "Optics and remote sensing of Bahamian carbonate sediment whiting and potential relationship to wind-driven Langmuir circulation," Biogeosciences **6**, 487–500 (2009).
13. M. S. Twardowski, H. Claustre, S. A. Freeman, D. Stramski, and Y. Huot, "Optical backscattering properties of the 'clearest' natural waters," Biogeosciences Disc. **4**, 2441–2491 (2007).
14. Z. Lee, K. P. Du, and R. Arnone, "A model for the diffuse attenuation coefficient of downwelling irradiance," J. Geophys. Res. **110**, C02016 (2005).
15. Z. Lee, R. Arnone, C. Hu, J. Werdell, and B. Lubac, "Uncertainties of optical parameters and their propagations in an analytical ocean color inversion algorithm," Appl. Opt. **49**, 369–381 (2010).
16. M. A. Montes-Hugo, K. Carder, R. J. Foy, J. Canizzaro, E. Brown, and S. Pegau, "Estimating phytoplankton biomass in coastal waters of Alaska using airborne remote sensing," Remote Sens. Environ. **98**, 481–493 (2005).
17. J. H. Churnside, J. J. Wilson, and V. V. Tatarski, "Airborne lidar for fisheries application," Opt. Eng. **40**, 406–414 (2001).
18. J. H. Churnside and J. J. Wilson, "Ocean color inferred from radiometers on low-flying aircraft," Sensors **8**, 860–876 (2008).
19. H. R. Gordon and M. Wang, "Retrieval of water-leaving radiance and aerosol optical thickness over the oceans with SeaWiFS: a preliminary algorithm," Appl. Opt. **33**, 443–552 (1994).
20. Z. Lee, B. Lubac, J. Werdell, and R. Arnone, "An update of the quasi-analytical algorithm (QAA_v5)," in *International Ocean Color Group Software Report* (2009), www.ioccg.org/groups/Software_OCA.
21. R. C. Smith and K. S. Baker, "Optical properties of the clearest natural waters (200–800 nm)," Appl. Opt. **20**, 177–181 (1981).
22. S. Sathyendranath and T. Platt, "The spectral irradiance field at the surface and in the interior of the ocean: a model for applications in oceanography and remote sensing," J. Geophys. Res. **93**, 9270–9280 (1988).
23. M. A. Montes-Hugo, J. H. Churnside, R. W. Gould, R. A. Arnone, and R. Foy, "Spatial coherence between remotely sensed ocean color data and vertical distribution of lidar backscattering in coastal stratified waters," Remote Sens. Environ. **114**, 2584–2593 (2010).
24. T. J. Petzold, "Volume scattering functions for selected ocean waters," SIO ref. 72–78, Scripps Institution of Oceanography, La Jolla, California, 1972.
25. V. I. Haltrin, M. E. Lee, V. I. Mankovsky, E. B. Shybanov, and A. D. Weidemann, "Integral properties of angular light scattering coefficient measured in various natural waters," in *Proceedings of the II International Conference Current Problems in Optics of Natural Waters*, I. Levin and G. Gilbert, eds. (2003), pp. 252–257.
26. K. L. Carder, F. R. Chen, Z. P. Lee, and S. K. Hawes, "Semianalytical Moderate-Resolution Imaging Spectrometer algorithms for chlorophyll a and absorption with bio-optical domains based on nitrate-depletion temperatures," J. Geophys. Res. **104**, 5403–5421 (1999).
27. E. J. D'Sa and D. S. Ko, "Short-term influences on suspended particulate matter distribution in the northern Gulf of Mexico: satellite and model observations," Sensors **8**, 4249–4264 (2008).
28. P. Wang, E. S. Boss, and C. Roesler, "Uncertainties of inherent optical properties obtained from semianalytical inversions of ocean color," Appl. Opt. **44**, 4074–4085 (2005).
29. Y. I. Kopelevich and A. G. Surkov, "Mathematical modeling of the input signals of oceanographic lidars," J. Opt. Technol. **75**, 321–326 (2008).
30. J. H. Churnside, "Polarization effects on oceanographic lidar," Opt. Express **16**, 1196–1207 (2008).
31. J. H. Churnside, "Lidar signature from bubbles in the sea," Opt. Express **18**, 8294–8299 (2010).
32. J. R. Zanaveld and S. Pegau, "Robust underwater visibility parameter," Opt. Express **11**, 2997–3009 (2003).